Engineering surface and morphology of La/WO_3 for electrochemical oxygen reduction

Swetha Ramani,[a] Zhewen Yin,[b] Bradley Miller,[c,†] Venkat R. Bhethanabotla,[a,b,c,*] John N. Kuhn[a,b,c,*]

[a] Department of Chemistry, University of South Florida, Tampa, Florida, 33620-5350

[b] Materials Science and Engineering Program, University of South Florida, Tampa, Florida, 33620-5350

[c] Department of Chemical & Biomedical Engineering, University of South Florida, Tampa, Florida, 33620-5350

Abstract: Altering the surface electronic properties of non-precious electrocatalysts via metal incorporation is an effective approach towards enhancing the oxygen reduction performance. Here, we explored the effect of introducing a rare-earth metal (La up to 20 mole %) in WO_3 using a novel crystal engineering strategy. Incorporation of La resulted in coalescence of randomly oriented nanoparticles directed towards one-dimensional growth into nanorods, exposing a preferential high catalytic active facet (002) of WO_3. Simultaneously, introduction of La induced the formation of oxygen vacancies at the surface, which coincided with increased hydroxyl adsorption. Benefitting from a combined effect of highly active facet and increased density of surface vacancies, 10% La exhibited two times higher current than pure WO_3. An improvement of 90 mV in onset potential highlights the prospects of La addition on electrochemical activity of metal oxides.

Keywords: oxygen reduction reaction, coalescence, Tafel slope, sol-gel, structure directing

Introduction

Advanced electrochemical energy systems such as fuel cells[1, 2] and air batteries[3] have high potential in clean energy conversion. Development of its large-scale industrial application is primarily limited due to high overpotentials involved with oxygen electrocatalysis. The concerning electrochemical reaction occurring at the cathode (oxygen reduction reaction – ORR) has sluggish reaction kinetics and requires the use of expensive catalysts like noble metals (Pt) to produce substantial amount of currents.[4, 5] Therefore, developing a durable high performance electrode using alternate cost effective materials can expand commercialization of these energy systems.[6] Towards this effort, low cost and high abundant transition metal based electrocatalysts such as metal oxides,[7, 8] phosphides,[9, 10] and chalcogenides[11-13] have demonstrated great potential as candidates for commercial electrode materials.

Metal oxides, especially, tungsten trioxide (WO_3) exhibit unique bulk and surface properties arising from its point defects. WO_3 is an indirect band gap semiconductor with a distorted low symmetry structure derived from cubic ReO_3. Its lattice consists of WO_6 octahedra formed by sharing oxygen atom at each corner and tungsten atom at the center.[14] The ability of tungsten to display various stable oxidation states is pertinent to stable electrocatalysts in a redox environment, hence demonstrating high stability as electrode materials.[15] Unlike other metal oxides

identified for ORR, study of WO_3 is limited as a support for noble metals due to its low surface area and electrical conductivity.[16-20] Current reports suggest superior electrocatalytic ORR activity of Pt/WO_3 due to uniform dispersion of smaller Pt-NPs (nanoparticles) and promotional effect between deposited Pt-NPs and WO_3 support.[21] This promotional effect arises due to strong interactions which help stabilize active Pt sites in a highly redox environment. Metal oxide supports act as a reservoir of oxygen species and help lower the overall reaction energy.[22] Another efficient method to enhance the electrocatalytic activity of WO_3 demonstrated by Cui *et. al.* showed 1.6 times larger current than Pd/C by alloying Pd and W ($Pd_{0.8}W_{0.2}$/C) and benefitted from employing bimetallic catalysts in tuning the active site electronic structure resulting in altered strength of chemisorbed oxygenated species and influence the overall catalytic performance.[23] Although incorporating noble metals in WO_3 based electrocatalysts is an effective approach, improving the ORR activity of WO_3 using alternate cheaper routes is of great significance.

To improve the electrochemical performance of WO_3 based catalysts, much effort has been done in devising novel nanostructures with high surface area. Recent study on La doped WO_3 demonstrated increased performance in photocatalytic conversion of CH_4 with 100% selectivity.[24] Though the effect of rare earth doping was highlighted in the article, there is a lack of detailed manipulation of accompanied morphological changes due to metal incorporation. Liu et al reported that incorporation of a rare earth metal Ce^{3+} in MnO_2 resulted in the agglomeration of particles to form sheets with almost 3 times higher surface area.[25] They correlated the advantages of metal doping to formation of oxygen vacancies (O_{vac}), at the crystal boundaries of the two oxides, resulting in higher catalytic performance. The extent of O_{vac}, achieved via interfacial strain and varying deposition conditions,[26] can tune the overall rate of electron transfer and reductive catalytic properties of WO_{3-x}.[27-29] However, the anisotropic trend of these properties along the most stable crystal facets of WO_3, i.e. (002), (020) and (200), highlight the importance of crystallographic preferential orientation.[30, 31] Changes in intrinsic electronic and band gap properties associated with each of these planes were employed as a tool to understand its photoelectrochemical properties.[31] Therefore, engineering the surface of WO_3 towards formation of O_{vac}, favoring preferential growth of catalytically active facet can tactically improve catalytic activity.

This work presents a novel strategy by incorporating a rare earth metal (La) into the WO_3 matrix using a template assisted sol gel technique. Insights on the growth mechanism of WO_3 NPs to preferentially exposing (002) in La/WO_3 NRs has been discussed. Incorporation of basic sites via lanthanum addition impacts the surface hydroxyl (OH_{ads}) coverage directly associating the amount of O_{vac} defects formed. A simultaneous effect resulting from preferential orientation of highly active (002) facet and O_{vac} sites offers promising enhancements in electrochemical oxygen reduction performance.

Experimental section

Chemicals.

Pluronic P-123 (Sigma Aldrich), tungsten chloride WCl_6 (Sigma Aldrich, >99.9%), anhydrous ethanol (Sigma Aldrich, <0.005% water), lanthanum nitrate hexahydrate $La(NO_3).6H_2O$ (Alfa aesar, 99.9%), 20% Pt/C (sigma Aldrich), tungsten trioxide powder (Sigma Aldrich,>99%) Vulcan XC72 (Cabot), Nafion (Sigma Aldrich). All Chemicals were used without any further purification.

Synthesis.

In a typical synthesis as reported by Yang et al, 10 g of Pluronic (P-123) and 100 g anhydrous ethanol were mixed and stirred until P-123 was completely dissolved.[32] WCl_6 (0.396 g) was added to the solution and stirred for 30 min. The solution turned yellow immediately and was left open in a beaker for aging at 40 °C for 7 days. The solution changed into a dark blue gel, W-P precursor. The W-P precursor was then calcined at 550 ℃ in the air for 4 hr. A minimum of 550 ℃ was required to obtain crystalline phase of monoclinic WO_3. La doped WO_3 samples were synthesized using the above described method. Different mole fractions of $La(NO_3)_3.6H_2O$ was added along with WCl_6 to obtain 5% La/WO_3, 10% La/WO3, 20% La/WO_3.

Materials Characterization.

The phase and structure of WO_3 samples (La = 0, 5, 10, 20%) were characterized by X-ray diffraction (Bruker/D8 Advance) using Cu anode target (λ=1.5418 Å). Pawley fit was performed to determine full width at half maxima (FWHM) and intensities of diffraction lines. The fit was done using the crystal structures of monoclinic WO_3 along with an additional heteropoly acid phase of tungsten. Morphology was initially analyzed by SEM-EDS using Hitachi S-800 Electron Microscope at an accelerating voltage of 25kV and working distance of 15mm. For EDS-color mapping, an accelerating voltage of 17 kV was applied. TEM studies of all catalysts were performed in a Tecnai F20 transmission electron microscope with accelerating voltage 200 kV and a point resolution of 0.24 nm. Specific surface areas were calculated from N_2 physisorption Brunauer-Emmet-Teller (BET) equation with an automated gas sorption analyzer (Quantachrome instruments), based on the data obtained within pressure range P/P_0 from 0.05 to 0.3. Surface analysis was done on catalysts using ULVAC- PHI XPS. The pass energy used for the individual peaks is 23.5 eV. The binding energy scale for the instrument was calibrated using the Au 4f7 peak at 84.0 eV. When data is taken from samples, C 1s peak is used as reference and is shifted to 284.8 eV with all the other data in the set shifted accordingly. The powder samples are placed on adhesive tape which insulates the powder from the grounded puck surface. This allows the powder to float to a uniform potential across its surface and an electron flood gun in conjunction with a low energy Ar ion beam to bring the surfaces to a uniform potential to eliminate differential charging. The

data is then calibrated during data processing by shifting the C 1s peak to 284.8 as mentioned above.

Electrochemical Studies.

The electrocatalytic ORR activity of all samples were tested using a rotating disk electrode (RDE) on Gamry Electrochemical workstation. A three-electrode setup consisting of glassy carbon as the working electrode, Pt wire as the counter electrode and a saturated calomel electrode as the reference electrode were employed. The electrode inks were prepared by dispersing 1.5 mg sample and 0.5 mg Vulcan in 500 µL isopropanol and 500 µL distilled water. Nafion (1 wt%; 10 µL) was added in the ink before sonicating for 30 min. Then, 20 µL was drop casted onto the RDE and dried in air. Prior to drop cast, electrodes were polished thoroughly using 0.05 µm alumina. The amount of catalyst on the RDE surface was kept constant for all samples at 0.04 mg. Industrial applications employing ORR requires either 0.1M KOH or very high 6M KOH (metal air batteries). We chose 1M KOH as a mid-ground, since common reference electrodes are not "leak-free" in 6M KOH.[33] 1M KOH electrolyte solution was purged with ultra-pure N_2 for 20 mins before starting the experiments. Cyclic voltammetry (CV) and linear sweep voltammetry (LSV) measurements were done at 50 mV/s and 5 mV/s respectively. Oxygen was bubbled throughout the experiment span. For analysis purpose, the potential range was converted to RHE using the equation, $E_{RHE} = E_{SCE} + 0.0591*pH$. To calculate the number of electrons transferred, Koutecky-Levich plot was obtained by running LSV at different rotation rates. Rotating ring disk electrode (RRDE) technique was employed to determine the amount of H_2O_2 produced in the same electrolyte solution. All experiments were performed in O_2 saturated 1 M KOH at 1600 rpm. RRDE current displayed are taken after 20 cycles of CV to stabilize the value of current. % H_2O_2 was calculated using the formula, $\%H_2O_2 = \frac{200\, I_r/N}{I_d+\frac{I_r}{N}}$ with a collection efficiency of 0.26.

Results and discussion

P-123 consisting of alternating hydrophobic (PPO) and hydrophilic (PEO) moieties was used as a template to synthesize WO_3 catalysts.[34] During aging process, hydrophilic PEO moiety forms a crown ether type complex with W^{6+} and La^{3+}, resulting in a gel formation.[35] After calcination of the gel at 550 ^oC, La/WO_3 (0, 5, 10 and 20%) catalysts exhibit sharp diffraction lines. A change in major diffraction line is observed for all catalysts from that of its reported monoclinic structure. Its corresponding d spacing is also verified from lattice fringes seen in HRTEM analysis as described later. WO_3 catalysts prepared in this technique is observed to exists in two monoclinic crystal phases - ε and γ. Pure WO_3 exhibits diffraction lines related to ε–WO_3, observed due to incomplete phase transition to thermodynamically favored γ–WO_3. Work done by Wang et. al. attributed this inhibition of thermodynamically favored phase transition to the diffusion of C from P123 into the interstitial sites, subsequently

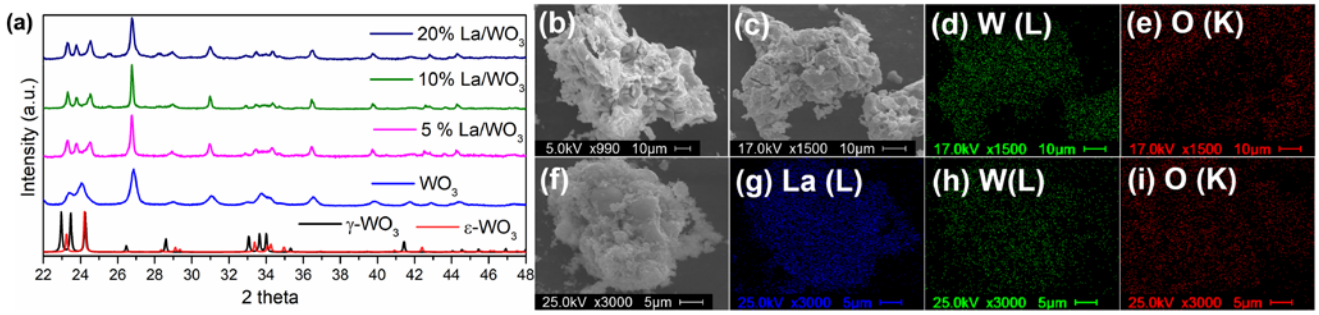

Figure 1. (a) PXRD of WO_3, 5% La/WO_3, 10% La/WO_3, 20% La/WO_3 and SEM images and elemental mapping of (b-e) WO_3, (f-i) 10% La/WO_3.

stabilizing ε–WO_3.[36] Incorporation of La into the WO_3 matrix dictates phase transformation thermodynamically resulting in the stable γ phase as shown in Figure 1a.[37, 38] The diffraction lines around 22-25°, corresponding to γ phase, develop explicitly into three individual components- (002), (020) and (200). Variation in full widths at half maximum (FWHM), intensity and peak position with La addition associate crystal structure evolution of WO_3. An initial sharp decrease in FWHM for all three lines is observed (Figure S1a), which saturates with further La addition. This narrowing of diffraction lines can indicate improved crystallinity with increase in La. Figure S1b shows consistent predominance in the relative intensity of (002) compared to (020) and (200) with varying La %, indicating that the crystal growth is favored along (002).[31] Trend in 2θ positions did not change much as a function of La addition (Figure S1c). Due to larger ionic radii of La^{3+} (1.18 Å) compared to W^{6+} (0.6 Å), La^{3+} is very likely to occupy the interstitial sites on the surface of WO_3, forming La-O-W bond.[24] At higher amounts, new diffraction lines appear at 25° (100) and 28° (101), marking the formation of La_2O_3 phase.[39] Although, small La_2O_3 peaks appear in the XRD pattern of 10% La, it is worth mentioning that majority of La still occupies the interstitial sites. However, the intensity of these peaks remarkably increases in 20% catalyst, indicating a complete phase separation. Arriving at the maximum possible La addition, prior to complete phase separation, can provide crucial insights in understanding the role of La in altering surface properties of WO_3.

Figure 1b-c, f shows SEM images of pure and 10% La catalyst displaying porous asymmetrical particles of the order of several tens of microns. Difference in the size among these is observed by comparing the scales in Figure 1b and f. Both micrographs indicate aggregation of smaller particles to form larger particles. Detailed particle size and surface area analysis was done by N_2 adsorption studies at 77 K. Specific surface area for all catalysts were determined from reversible isotherms as shown in Figure S2a. Surface area calculated by BET method showed a 172% increase over pure WO_3 (11.3 m^2/g) for 5% La (31.0 m^2/g). This is due to reduction in particle size arising from blocked grain boundaries of WO_3 by La occupied interstitial sites. With higher amounts of La, a slight decrease

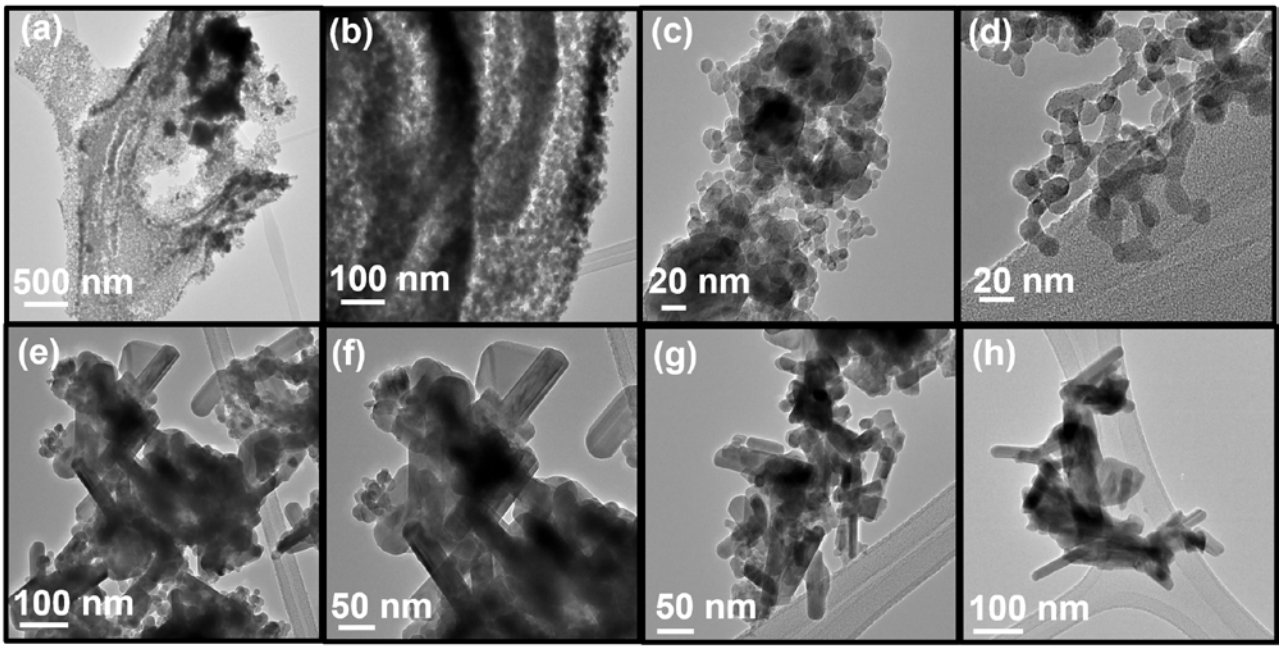

Figure 2. TEM image of La/WO3 - 0%: a,b; 5%:c,d; 10%: e,f and 20%: g,h.

in surface area occurs for 10% (24.6 m^2/g) and 20% (23.4 m^2/g). The surface area trend is also in consistent with the pore size distribution (Figure S2b). Number of pores increase with 5% La, owing to the reduction in the particle size. However, with more La incorporated into WO_3, pore volume decreases for 10 and 20%. Uniform elemental distribution is shown in the mapping image (1d-e, h-i) for WO_3 and 10% La/WO_3.

To further our understanding of the morphology of La/WO_3 catalysts and its trends in surface area and particle size reduction, TEM was utilized. Pure WO_3 displays a highly porous aggregation of particles with no definite shape. With 5% addition of La, small spheres with a size of ~13 nm are formed as shown in Figure 2c. Average size of these nanoparticles (NPs) was obtained from a bar graph distribution of 100 NPs (Figure S3), exhibiting sizes in the range of 10-14 nm. This reduction in particle size validates the increase in surface area obtained from BET method. A higher magnification shows coalescence (Figure 2d) of adjacent spherical NPs to form the seeds of elongated nanorods (NRs). With further La increase to 10 (Figure 2e, f) and 20% (Figure 2g, h), fully formed NRs of varying size appear, along with few NPs. The width of these NRs is about 13-16 nm, indicating one dimensional growth of NPs. The ratio of rods to NPs increases with La addition, highlighting its role in the morphological changes of these catalysts. Elemental analysis was performed on these NRs to confirm the presence of La, W and O, at high magnifications using STEM-EDS as shown in Figure S4. The HRTEM images taken on pure WO_3 NPs selectively expose the (021) plane, corresponding to the major diffraction line observed in PXRD (Figure S5a). We further revealed the growth mechanism of NPs to NRs of La/WO_3 catalysts, with increasing La amounts, using

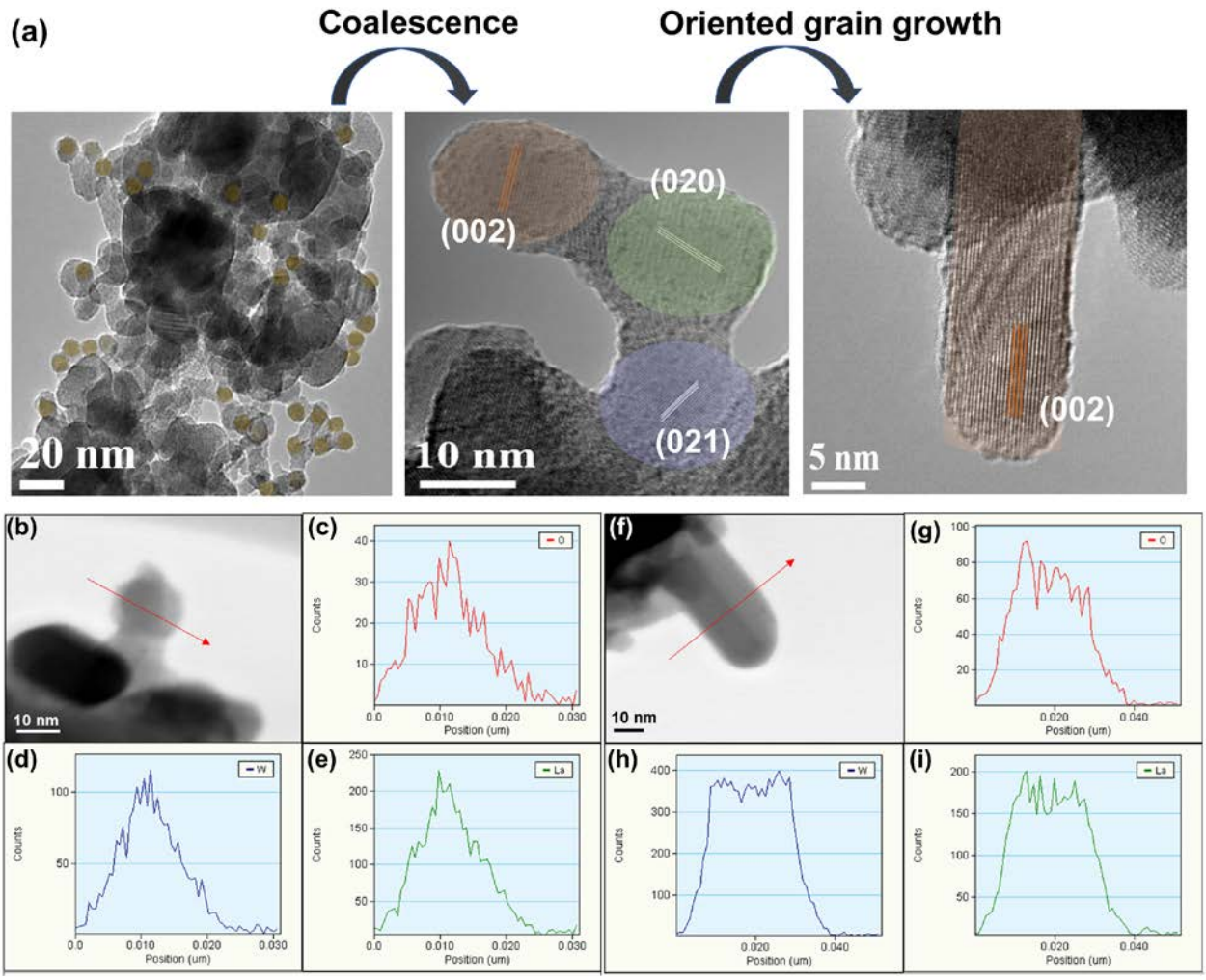

Figure 3. (a) Growth mechanism of WO_3 NPs into NRs, (b-e) EDS Line scan on La doped WO_3 NPs showing O (Kα), W (M) and La (Lα) profiles, (f-i) EDX Line scan on La doped WO_3 NRs showing O (Kα), W (M) and La (Lα) profiles.

HRTEM analysis. In general, it is known that doping technique results in decrease in particle size along with higher surface area. Introducing La creates grain boundaries during synthesis, restraining the growth of WO_3 particles resulting in NPs. At this stage, high magnification TEM images of 5% La/WO_3 shows coalescence of adjacent NPs to form dumbbell shaped structures (Figure 3a). Lattice fringes of three different planes - (002), (020) and (021) are observed, indicating self-assembly of randomly orientated NPs. Subsequently, the next growth stage is kinetically controlled by adsorption of precursors on different planes. In the case of La addition into WO_3, it is important to note the presence of NO_3^- ions from La precursors which favors strong adsorption on (002) plane of WO_3, inhibiting the growth in that direction resulting in predominantly exposing (002) facet.[30] Apart from nitrate ions, introducing metal dopants is also seen to influence the growth kinetics of NPs by favoring growth along a particular direction. Recent work on the effects of cobalt doping on the growth of ZnO nanorods demonstrated a delay in the growth of

NPs in all directions and favoring sideways growth along c-axis.[40, 41] Therefore, with higher presence of La^{3+} and NO_3^- ions, self-assembled La/WO_3 NPs grow along one direction selectively exposing (002) crystallographic plane.

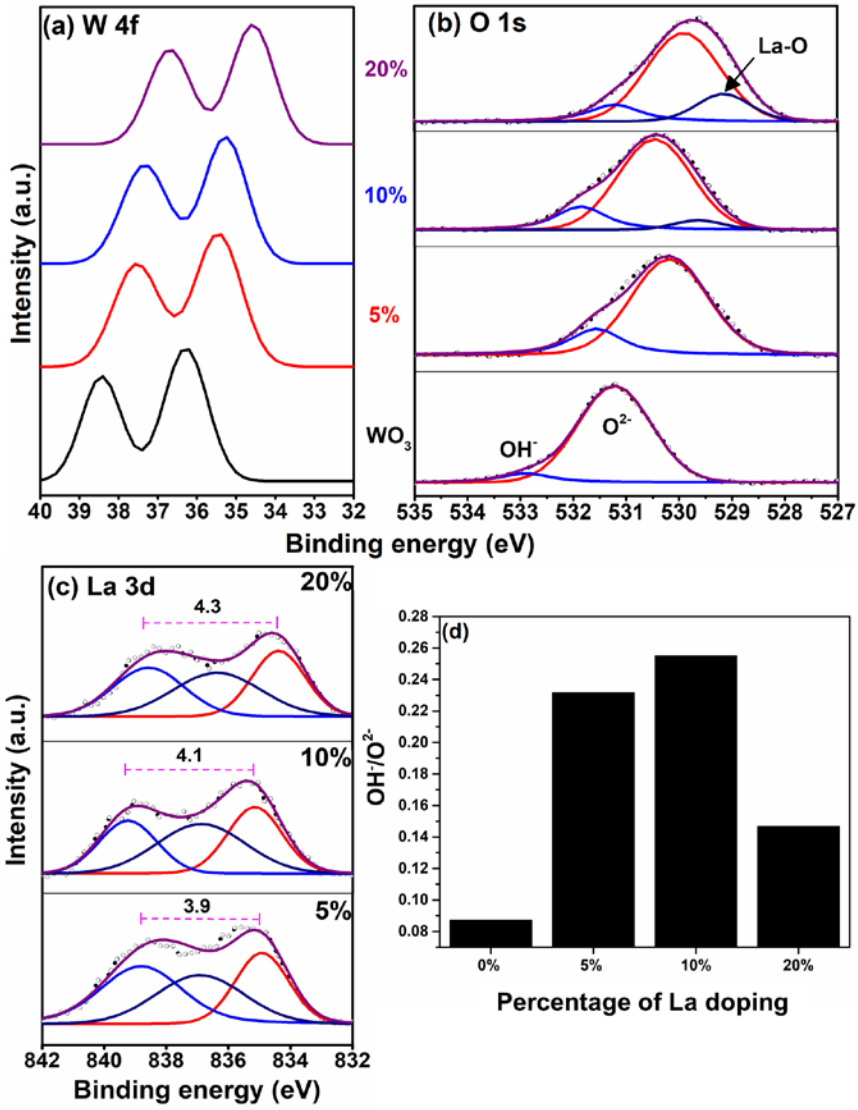

Figure 4. XPS profiles of (a) W 4f, (b) O 1s, (c) La 3d and (d) OH^-/O^{2-} calculated for different catalysts from area of the peak component.

The significance of synthesizing preferentially (002) exposed WO_3 due to its high surface energy (1.56 Jm^{-2}) was highlighted by Zhang and his coworkers demonstrating favorable adsorption of active oxygen species resulting in excellent photoelectrochemical water splitting performance.[42] The preferential orientation in WO_3 monoclinic structure arises due to smaller lattice parameters of (002) plane, thereby, forming a closely packed plane. Due to this high density of atom arrangement (00a) family planes have shown to exhibit higher catalytic activity.[43, 44] Therefore, by altering La amounts, morphology selective exposure of a single facet in La/WO_3 catalysts was successfully achieved. STEM-EDS analysis shows the distribution of La in both WO_3 NPs (Figure 3(b-e)) and NRs (Figure 3(f-i)) confirming that La is well embedded onto WO_3 matrix.

IR spectra of all catalysts is shown in Figure S5b, clearly indicating characteristic bands pertaining to O-W-O and W=O. A slight OH_{str} is seen around 3500 cm^{-1} in La/WO_3, suggesting possible OH^- adsorption properties due to introduction of La^{3+} basic sites. To further understand the changes in surface properties, all catalysts were analyzed using XPS technique. Typical W 4f peaks corresponding to W^{6+} in WO_3 were observed in the region 32-40 eV (Figure 4a). Two characteristic peaks corresponding to the spin orbit coupling of W 4f, i.e. $4f_{5/2}$ and $4f_{7/2}$, showed a continuous shift towards lower binding energy (from 36.2 eV to 34.5 eV) with increase in La. This can be attributed to the presence of less electronegative La^{3+} (EN - 1.1), compared to W^{6+} (EN – 2.3). La incorporation into the WO_3 matrix particularly occurs only at the interstitial sites on the surface due to its larger size. At the interface of La/WO_3, instead of W-O-W, W-O-La can be expected resulting in decrease in bonding energy of W-O. A similar trend was demonstrated by Zhang using Fe-doped WO_3 displaying negative shifts in W spectra.[45] O 1s spectra had the most significant changes with increasing rare earth interaction. Deconvolution of O 1s spectra revealed two peaks for pure WO_3 corresponding to lattice O^{2-} and OH^- (Figure 4b). At 5% La, a significant increase in OH_{ads} arises due to favorable La-OH formation in undercoordinated La sites at the surface of WO_3. For increased La amounts, a new peak appears at lower binding energy (529.64 eV) indicating the formation of La-O.[46] The lattice O^{2-} peak of La_2O_3 appears at much lower binding energy due to low electronegativity of La^{3+}. This peak intensifies and shifts negatively to 529.1 eV at 20% La, confirming the complete phase separation of La_2O_3 as seen in PXRD. XPS analysis of La 3d was performed with reference to the work done by Sunding et al.[47] Deconvolution was done by imposing several constrains to the peak fitting parameters. Inspection of La 3d shows spin orbit components - $3d_{3/2}$ and $3d_{5/2}$ around 832-841 eV. The difference in energy (ΔE) between these peaks indicates if La is present as $La(OH)_3$ (3.9 eV) or La_2O_3 (4.6 eV). For 5% La, ΔE has a value of 3.9 eV implying that La at the surface exists as $La(OH)_3$.[48] An increase in ΔE to 4.1 (10%) and 4.3 eV (20%) suggests the possible presence of La as both $La(OH)_3$ and La_2O_3. One interesting feature observed with La increments was in the trend of surface OH^-/ lattice O^{2-} (Figure 3d). Amount of surface hydroxyl adsorption in metal oxides can be directly related to surface oxygen vacancies formed. With the introduction of lower valent La^{3+} into WO_3 matrix, charge neutrality is balanced by the formation of anion vacancy defect sites at the surface. Tuning the extent of La incorporation alters the amount of surface O_{vac} sites that can accommodate water molecules, thus altering the intensity of OH^-/O^{2-} ratio.[24] An increase in the amount of OH_{ads} observed at 5 and 10% La indicates higher O_{vac} sites at the surface. Recent work by two groups Liu *et. al.* and Jia *et. al.* found a similar effect in Ce/MnO_2 and α,γ-MnO_2 respectively, where increase in adsorbed species were observed in oxides with high density of oxygen vacancies.[25, 49, 50] However, due to secondary La_2O_3 phase at 20% La, the percentage of lattice oxygen rises. This results in decreased surface oxygen adsorbed species suggesting lower amount of oxygen vacancies. Thus, along with one dimensional growth of WO_3 NPs with (002)

facet, we modified surface properties of WO_3 with hydroxyl coverage and vacancies.

Insights from various characterization techniques employed on La/WO_3 catalysts, i.e particle size and morphology, surface hydroxyl coverage and facets, define the effects of La in electrochemical ORR performance. To investigate this, CV curve was taken in N_2 as well as O_2 saturated electrolyte. ORR in alkaline medium can either occur via a $4e^-$ or a $2e^-$ transfer process involving adsorption and desorption of various species like O^{2-}, O_2^2,

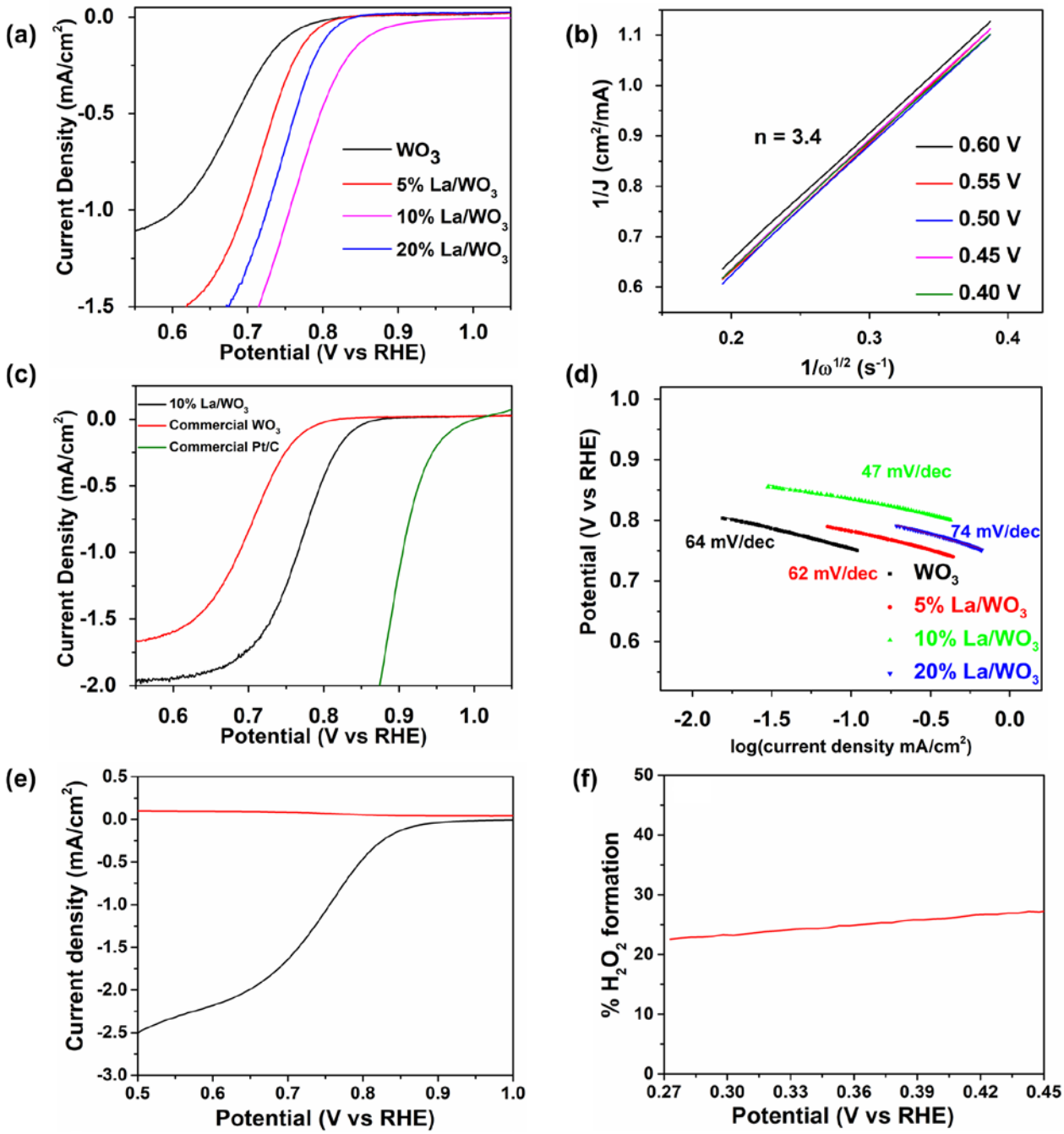

Figure 5. (a) Alkaline ORR activity represented in LSV curves of La/WO_3 (0, 5, 10, 20%) after 20 cycles in O_2 atmosphere, (b) KL plot of 10% La/WO_3 showing the total number of electrons transferred, (c) Comparison of 10% La/WO_3 with commercial WO_3 and 20% Pt/C, (d) Tafel slopes of La/WO_3 (0, 5, 10, 20%), (e) RRDE current of 10% La/WO_3 in O_2 saturated atmosphere , (f) % H_2O_2 formed during oxygen reduction on 10% La/WO_3.

OH^-, HO_2^-. The sudden increase in the cathodic current at 0.84 mV (Figure S5) verified the potential active sites of WO_3 for oxygen reduction. A comparison of ORR performance for La/WO_3 – 0, 5, 10, 20% is shown in Figure 6a. Pure WO_3 exhibited a low onset potential of 0.81 V, followed by 5% La at 0.84 V and 20% La 0.86 V. Best performance was exhibited by 10% La with an onset of 0.90 V. A similar trend in specific activity (mA/cm^2) was observed for all La/WO_3 catalysts with respect to BET surface area, indicating that BET technique potentially overestimates the electrocatalytic active surface area.[51] This remarkable onset potential can be elucidated using combination effect caused by surface hydroxyl adsorption induced by vacancy defects leading to unrestricted diffusion of oxygen to the WO_3 active sites. Beginning with 5% catalyst, though the effect of La addition is seen influencing the onset by a positive 30 mV shift, it is not enough to affect the reaction considerably. This could arise due to exposure of fewer catalytically active (002) facets constraining the adsorption of reactant oxygen species, as described earlier. Although 20% La exhibits NRs with (002) facet, low specific surface area and amounts of oxygen vacancies results in decreased performance. Therefore, due to optimal active sites and high vacancy defects at the surface for direct adsorption of oxygen reactant molecules, 10% La shows the best ORR performance. A Koutecky-Levich (KL) analysis was conducted to evaluate the number of electrons transferred (Figures 5b and S7). Pure WO_3 exhibited lowest number of electrons transferred (3.0) followed by, 20% La/WO_3 (3.1) < 5% La/WO_3 (3.2) < 10% La/WO_3 (3.4). This trend is in accordance to the amount of oxygen vacancy in a catalyst. Introduction of oxygen vacancies enables intrinsic mobility of electrons within the catalyst resulting in enhanced rate of electron transfer. This also corroborates with the lowest Tafel slope of 10% La (47 mV/dec) with the final 4^{th} electron transfer as the rate determining step(Figure 5d), followed by 5% (62 mV/decade) and pure WO_3 (64 mV/decade).[52] 20% La/WO_3 (74 mV/decade) showed the highest Tafel slope indicating a larger overpotential required for ORR as expected. Standard error in ORR potential were calculated from three experimental measurements for all catalysts (Figure S8). Employing RRDE technique on 10% La/WO_3, % H_2O_2 was determined to be around 20-30% during the reduction process (Figure 5e, f). This indicates that the ORR process occurs via a mixed 4 and 2 e- pathway on these catalysts. However, most of the conversion still proceeds via 4 electron transfer. To compare the ORR activity of 10% La/WO_3, commercial Pt/C and WO_3 were tested under the same experimental conditions (Figure 5c). The activity of 10% La/WO_3, showed considerable improvement when compared to WO_3. Though the activity is lower than Pt/C, we have demonstrated the potential of WO_3 for the first time as a non-noble metal catalyst with potential in electrochemical oxygen reduction reactions.

Conclusions

The effect of surface engineering and vacancy formation by rare earth incorporation into WO_3 was achieved. The resultant catalysts exhibited >100% increase in active surface area and reduction in particle size to ~ 13 nm.

Employing a simple sol-gel technique, preferential orientation of (002) facet on La/WO_3 catalysts is presented with a growth mechanism involving coalescence of NPs to form NRs. 10% showed highest activity with an onset of 0.90 V (vs RHE) and a low Tafel slope of 47 mV/decade. This enhancement in catalytic activity is attributed to exposure of highly active (002) plane as seen in TEM images and surface hydroxyl coverage signaling the high amounts of oxygen vacancies derived from XPS results. This work highlights the promising effects of tuning surface and morphology via rare earth (La) addition towards enhancing the ORR performance of metal oxides.

Acknowledgements

Funding from the National Science Foundation grant number is EEC-1560303 gratefully acknowledged. Authors also acknowledge Mr.Eric Lambers for his help in XPS measurements and Dr.Lukasz Wojitas for XRD analysis.

† Currently a student at New Mexico Tech

References

1. O. Gröger, H. A. Gasteiger and J.-P. Suchsland, *Journal of The Electrochemical Society*, 2015, **162**, A2605-A2622.
2. K. I. Ota, A. Ishihara, S. Mitsushima, K. Lee, Y. Suzuki, N. Horibe, T. Nakagawa and N. Kamiya, *Journal of New Materials for Electrochemical Systems*, 2005, **8**, 25-35.
3. Y. Li and J. Lu, *ACS Energy Letters*, 2017, **2**, 1370-1377.
4. C. Zhang, X. Shen, Y. Pan and Z. Peng, *Frontiers in Energy*, 2017, **11**, 268-285.
5. F. van Schalkwyk, G. Pattrick, J. Olivier, O. Conrad and S. Blair, *Fuel Cells*, 2016, **16**, 414-427.
6. X. Ge, A. Sumboja, D. Wuu, T. An, B. Li, F. W. T. Goh, T. S. A. Hor, Y. Zong and Z. Liu, *ACS Catalysis*, 2015, **5**, 4643-4667.
7. T. Greiner Mark, L. Chai, G. Helander Michael, W.-M. Tang and Z.-H. Lu, *Advanced Functional Materials*, 2012, **22**, 4557-4568.
8. Z. Zhang, J. Liu, J. Gu, L. Su and L. Cheng, *Energy & Environmental Science*, 2014, **7**, 2535-2558.
9. K. Chen, X. Huang, C. Wan and H. Liu, *RSC Advances*, 2015, **5**, 92893-92898.
10. F. Razmjooei, C. Pak and J.-S. Yu, *ChemElectroChem*, 2018, **5**, 1985-1994.
11. K. Lee, N. Alonso-Vante and J. Zhang, *Non-Noble Metal Fuel Cell Catalysts*, 2014, DOI: doi:10.1002/9783527664900.ch4
10.1002/9783527664900.ch4.
12. N. A. Vante, W. Jaegermann, H. Tributsch, W. Hoenle and K. Yvon, *Journal of the American Chemical Society*, 1987, **109**, 3251-3257.
13. Y. Feng, A. Gago, L. Timperman and N. Alonso-Vante, *Electrochimica Acta*, 2011, **56**, 1009-1022.
14. T. Vogt, P. M. Woodward and B. A. Hunter, *Journal of Solid State Chemistry*, 1999, **144**, 209-215.
15. R. S. Lillard, G. S. Kanner and D. P. Butt, *Journal of The Electrochemical Society*, 1998, **145**, 2718-2725.
16. Z. Zhang, X. Wang, Z. Cui, C. Liu, T. Lu and W. Xing, *Journal of Power Sources*, 2008, **185**, 941-945.
17. M. Dou, M. Hou, Z. Li, F. Wang, D. Liang, Z. Shao and B. Yi, *Journal of Energy Chemistry*, 2015, **24**, 39-44.
18. C. a. Ma, Y. Jin, M. Shi, Y. Chu, Y. Xu, W. Jia, Q. Yuan, J. Chen, D. Chen and S. Chen, *Journal of The Electrochemical Society*, 2014, **161**, F246-F251.
19. T. Y. Ma, Y. Zheng, S. Dai, M. Jaroniec and S. Z. Qiao, *Journal of Materials Chemistry A*, 2014, **2**, 8676-8682.
20. D. A. Kuznetsov, B. Han, Y. Yu, R. R. Rao, J. Hwang, Y. Román-Leshkov and Y. Shao-Horn, *Joule*, 2018, **2**, 225-244.
21. Z. Yan, W. Wei, J. Xie, S. Meng, X. Lü and J. Zhu, *Journal of Power Sources*, 2013, **222**, 218-224.
22. Z. Yan, J. Xie, J. Jing, M. Zhang, W. Wei and S. Yin, *International Journal of Hydrogen Energy*, 2012, **37**, 15948-15955.

23. N. Cui, W. Li, Z. Guo, X. Xu and H. Zhao, *Catalysts*, 2018, **8**.
24. K. Villa, S. Murcia-López, J. R. Morante and T. Andreu, *Applied Catalysis B: Environmental*, 2016, **187**, 30-36.
25. Y. Liu and P. Zhang, *Applied Catalysis A: General*, 2017, **530**, 102-110.
26. K. H. L. Zhang, G. Li, S. R. Spurgeon, L. Wang, P. Yan, Z. Wang, M. Gu, T. Varga, M. E. Bowden, Z. Zhu, C. Wang and Y. Du, *ACS Applied Materials & Interfaces*, 2018, **10**, 17480-17486.
27. T. Zheng, W. Sang, Z. He, Q. Wei, B. Chen, H. Li, C. Cao, R. Huang, X. Yan, B. Pan, S. Zhou and J. Zeng, *Nano Letters*, 2017, **17**, 7968-7973.
28. Z.-F. Huang, J. Song, L. Pan, X. Zhang, L. Wang and J.-J. Zou, *Advanced Materials*, 2015, **27**, 5309-5327.
29. T. Tuvić, I. Pašti and S. Mentus, *Russian Journal of Physical Chemistry A*, 2011, **85**, 2399-2405.
30. Y. P. Xie, G. Liu, L. Yin and H.-M. Cheng, *Journal of Materials Chemistry*, 2012, **22**, 6746-6751.
31. W. L. Kwong, P. Koshy, Judy N. Hart, W. Xu and C. C. Sorrell, *Sustainable Energy & Fuels*, 2018, **2**, 2224-2236.
32. P. Yang, D. Zhao, D. I. Margolese, B. F. Chmelka and G. D. Stucky, *Nature*, 1998, **396**, 152-155.
33. C. Alegre, A. Stassi, E. Modica, C. Lo Vecchio, A. S. Aricò and V. Baglio, *RSC Advances*, 2015, **5**, 25424-25427.
34. Q. Liang, X. Guo, T. Quan and F. Meng, *Journal of Advanced Ceramics*, 2016, **5**, 225-231.
35. P. Yang, D. Zhao, D. I. Margolese, B. F. Chmelka and G. D. Stucky, *Chemistry of Materials*, 1999, **11**, 2813-2826.
36. D. Wang, S. Huang, H. Li, A. Chen, P. Wang, J. Yang, X. Wang and J. Yang, *Sensors and Actuators B: Chemical*, 2019, **282**, 961-971.
37. X. Cui, J. Shi, H. Chen, L. Zhang, L. Guo, J. Gao and J. Li, *The Journal of Physical Chemistry B*, 2008, **112**, 12024-12031.
38. H. Zheng, J. Z. Ou, M. S. Strano, R. B. Kaner, A. Mitchell and K. Kalantar-zadeh, *Advanced Functional Materials*, 2011, **21**, 2175-2196.
39. J.-G. Kang, Y.-I. Kim, D. Won Cho and Y. Sohn, *Materials Science in Semiconductor Processing*, 2015, **40**, 737-743.
40. M. Ali, S. Sharif, S. Anjum, M. Imran, M. Ikram, M. Naz and S. Ali, *Materials Research Express*, 2020, **6**, 1250d1255.
41. F. C. Kartawidjaja, Z. Y. Lim, S. L. G. Ng, Y. Zhang and J. Wang, *Journal of the American Ceramic Society*, 2010, **93**, 3798-3802.
42. J. Zhang, P. Zhang, T. Wang and J. Gong, *Nano Energy*, 2015, **11**, 189-195.
43. D. Zhang, S. Wang, J. Zhu, H. Li and Y. Lu, *Applied Catalysis B: Environmental*, 2012, **123-124**, 398-404.
44. Y. Guo, X. Quan, N. Lu, H. Zhao and S. Chen, *Environmental Science & Technology*, 2007, **41**, 4422-4427.
45. T. Zhang, Z. Zhu, H. Chen, Y. Bai, S. Xiao, X. Zheng, Q. Xue and S. Yang, *Nanoscale*, 2015, **7**, 2933-2940.
46. B. M. Reddy, B. Chowdhury and P. G. Smirniotis, *Applied Catalysis A: General*, 2001, **219**, 53-60.
47. M. F. Sunding, K. Hadidi, S. Diplas, O. M. Løvvik, T. E. Norby and A. E. Gunnæs, *Journal of Electron Spectroscopy and Related Phenomena*, 2011, **184**, 399-409.
48. A. B. Yousaf, M. Imran, M. Farooq and P. Kasak, *Sci. Rep.*, 2018, **8**, 4354.
49. J. Jia, P. Zhang and L. Chen, *Applied Catalysis B: Environmental*, 2016, **189**, 210-218.
50. X. Li, J. Ma, L. Yang, G. He, C. Zhang, R. Zhang and H. He, *Environmental Science & Technology*, 2018, **52**, 12685-12696.
51. S. Jung, C. C. L. McCrory, I. M. Ferrer, J. C. Peters and T. F. Jaramillo, *Journal of Materials Chemistry A*, 2016, **4**, 3068-3076.
52. T. Shinagawa, A. T. Garcia-Esparza and K. Takanabe, *Sci. Rep.*, 2015, **5**, 13801.

TOC:

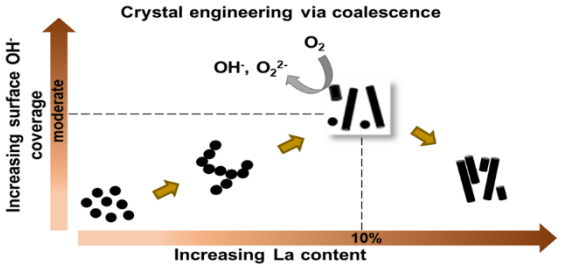
Crystal engineering via coalescence
O2
OH-, O2 2-
Increasing surface OH- coverage
moderate
10%
Increasing La content